

Electro-acoustic control of radiation impedance for brass instrument timbre shaping: design of a vocalizing mute

Vincent Martos^{1,*}, Henri Boutin¹, Thomas Hélie², and Brigitte d'Andréa-Novel³

¹S3AM-STMS-Sorbonne Université-Ircam, 1, Place Igor Stravinsky, 75004 Paris, France

²S3AM-STMS-CNRS-Ircam, 1, Place Igor Stravinsky, 75004 Paris, France

³Mines Paris – PSL, Center of Robotics, 60 bd Saint-Michel, 75006 Paris, France

Received 20 August 2024, Accepted 10 May 2025

Abstract – The application of active control to musical instruments brings many benefits to composers and performers, by expanding their sound possibilities. This paper addresses the active control of a brass instrument to design a vocalizing mute. To this end, a sensor (pressure transducer) and an actuator (loudspeaker) with a feedback loop are placed at the bell extremity. A single-input single-output controller is designed to simulate the insertion of a flow-to-flow vocal filter, upstream of the natural radiation impedance load. The vocal transfer function with its target resonances is basically derived using the transfer matrix method for a vocal tract composed of concatenated acoustic cylinders. The loudspeaker model is based on the Thiele and Small description. Numerical experiments are presented on the controller, for a simplified trombone model that admits a Kelly-Lochbaum structure (mouthpiece, bore, bell and radiation are cascaded using the transfer matrix method). Finally, the sensitivity of the control to air temperature, bell opening angle and loudspeakers parameters is studied.

Keywords. Active control, Augmented brass instrument, Formants

1 Introduction

Active control serves as a versatile technique for modifying the vibrations of a system through the use of transducers. It was first used in noise reduction (cf. Lueg patent to suppress pure tones in pipes [1], Fogel for noise reduction in aircraft cockpits [2]). It has also been used for several years on musical instruments enabling the creation of so-called augmented instruments. The first piano with an active control system was patented in 1893 [3] by Eisenmann, on which a controller extended the string vibration using electromagnets. Feedback controllers based on the same principle have been developed more recently for electric guitar strings [4, 5]. In the family of percussion instruments, active modal control has also been developed to control the vibration modes of a xylophone bar [6]. Concerning wind instruments, active control has been used to modify the input impedance of a clarinet [7] and to study nonlinear couplings with its resonator [8]. This paper is part of the general study of active control applied to brass instruments.

Playing vowels with instruments can produce a spectacular effect, for example with hand movements in front of a trombone bell in the manner of a Kempelen

machine [9], or with dedicated mutes, as in the case of S. Turre or P. Eötvös in the piece *Snatches of Conversation*, who uses an association of Pixie and Plunger mutes. Also, using active control to modify the sound of brass instruments has a number of advantages. Thus, during performance, a brass player naturally controls his instrument through auditory feedback (radiated sound) and haptic feedback (felt through the vibration of his lips), which are correlated. By using active control, which allows the instrument to produce new sounds by modifying its own vibration (that of its air column), this correlation is preserved. This is in contrast to usual sound effects, which act on recorded sound and then play it back through loudspeakers. For these two reasons, this study aims to design a vocalizing mute using active control. To do that, we propose to modify the radiation impedance of a trombone, in order to simulate the presence of a human vocal tract downstream of its resonator. The choice of the geometry of the simulated vocal tract will make it possible to produce new trombone sounds by applying a spectral envelope similar to that of human vowel sounds. This article follows on from [10], which presents the first theoretical results. The simulations are improved using a Kelly-Lochbaum structure, and an analysis of the controller sensitivity is added.

*Corresponding author: vincentmartos@hotmail.fr

The paper is organised as follows. [Section 2](#) presents a global block diagram of the instrument (from the performer’s mouth cavity to the acoustic radiation), introduces the control block inserted to achieve the objective, and sets out the working hypotheses on which the control law will be designed. [Section 3](#) details basic passive acoustic modellings of radiation impedance and of the vocal tract to be virtualised. They are presented in the spectral domain (Laplace and Z). [Section 4](#) is devoted to the design of the acoustic control law that achieves the target behaviour. It also examines its robustness through a sensitivity analysis. Then, [Section 5](#) focuses on the sensors and actuators. It introduces their modelling with parameters and then derives the electro-acoustic feedback law to be implemented between these transducers. Finally, [Section 6](#) presents numerical experiments and discusses the impact of the active control method developed in this article on the waveform and spectrum of the radiated sound.

2 Problem statement

This section sets out the work basis chosen in this paper to modify a trombone and make it radiate vowels.

It describes the played instrument in the form of a block diagram ([Sect. 2.1](#)) used to formulate the objective ([Sect. 2.2](#)) and the working hypotheses ([Sect. 2.3](#)). It then presents the control structure ([Sect. 2.4](#)), on the basis of which the control law will be designed ([Sect. 2.5](#)).

2.1 Structure of a played trombone and acoustic elements

Addressing the control of the trombone under realistic playing conditions requires consideration of several working constraints, such as:

- (C1) complex aero-acoustic coupling with lips [11, 12],
- (C2) complex modelling of visco-thermal losses inside the pipe [13–17],
- (C3) both longitudinal and transverse modes above approximately 1250 Hz (see [18, Fig. 4]), which overlap the frequency range of the targeted application (the first four vowel resonances typically lying between 250 Hz and 4 kHz),
- (C4) time-varying length due to slide movements when playing,
- (C5) nonlinear propagation at high playing levels (see [19, 20] for modelling and [21] for sound synthesis).

This is witnessed by many studies and a large literature; see, e.g., [22] and the references therein.

To address these constraints and prepare an effective control strategy, the instrument is first decomposed into several blocks, as shown in [Figure 1](#):

Block A represents the complex dynamical system composed of the performer excitation coupled to the

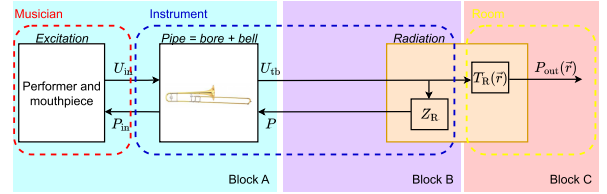


Figure 1. Block diagram of a played trombone in its environment. First, the pipe is described by a quadripole. The two inputs are the mouthpiece volumetric flow rate, denoted U_{in} and the pressure at the bell, denoted P . The two outputs are the flow rate at the bell, U_{tb} and the mouthpiece pressure P_{in} . Second, the radiation is represented by a linear impedance load Z_R (equal to P/U_{tb} in the Laplace domain). And the transfer impedance $T_R(\mathbf{r})$ between U_{tb} and the pressure $P_{out}(\mathbf{r})$ at a point \mathbf{r} . Note that in all the paper, flow rates are algebraic quantities counted positively in the direction of \mathbf{e}_ℓ (e.g., $\mathbf{U}_{in} = U_{in}\mathbf{e}_\ell$).

acoustic bore until the acoustic state (pressure, air-flow) at the bell extremity,

Block B represents the radiation load experienced by this state at the bell extremity,

Block C represents how this state propagates into the room, including directivity effects.

[Figure 1](#) also introduces notations and conventions used within this paper.

2.2 Objective

Our objective is to develop a control method that operates effectively and independently of constraints (C1)–(C5) to make the trombone radiates vowels.

Strategy. We choose to work only on block B, by introducing a controller with a feedback loop, as proposed in [Figure 2](#): the natural bell flow U_{tb} is augmented by an additional component U_{ac} for reshaping the radiation load, using a control, to meet a target. In the block diagram, this insertion is acoustically implemented at the isobar located at the bell extremity (see hypotheses below). It operates as a conservative junction with three ports, all of which share the same pressure and effectively balances all incoming flow rates. Following the orientation convention for flow rates, this balance equation reads $U_R = U_{ac} + U_{tb}$.

Target. In this paper, active control is used to simulate the presence of a vocal tract downstream of the trombone resonator, an organ that, in humans, extends from the glottis to the buccal cavity. Here, the nasal cavity is assumed to be closed by the soft palate, which allows only nonnasal vowels to be produced. The vocal tract is therefore considered an unbranched tube with a single input, the incoming flow rate on the glottis side, and a single output, the outgoing flow rate on the lips side. As the simulated vocal tract is placed at the output of the trombone resonator, according to the notations shown in

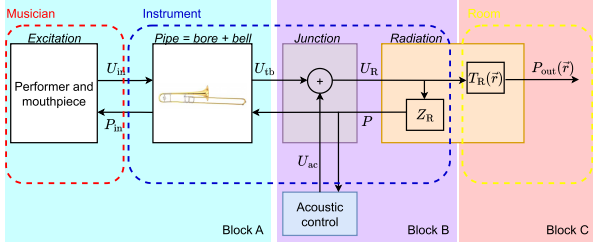


Figure 2. Block diagram of the musical instrument equipped with active control. Note that with no control ($U_{ac} = 0$), we recover the Figure 1 ($U_R = U_{tb}$).

Figure 2, these two flow rates are equal to U_{tb} and U_R respectively. The goal is to modify the radiated airflow as

$$U_R = H_{VT} \cdot U_{tb}, \quad (1)$$

where H_{VT} represents the vocal tract transfer function in the Laplace domain, that relates the airflow at the glottis to the airflow at the lips for a given vowel.

2.3 Hypotheses

The following assumptions are made, focusing exclusively on Block B in alignment with the strategy and objective:

- (H1) **Radiation load:** approximated by a linear time-invariant passive impedance on a spherical cap (model chosen in Sect. 3.1);
- (H2) **Vocal tract (target):** modeled by a linear time-invariant transfer function that relates the airflow at the glottis to the airflow at the lips (model chosen in Sect. 3.2);
- (H3) **Controller:** linear time invariant feedback-loop between transducers (sensors and actuators) also assumed to be linear (design in Sects. 2.4 and 5.2). In this theoretical study, transducers are supposed to be co-located and distribute a homogeneous acoustic control over the spherical cap.

2.4 Control structure

The overall structure of the controller is shown in Figure 3. As explained in the objective, in Section 2.2, it takes the bell pressure as its only input. According to hypothesis of co-located control (H3), the loudspeaker generates a contribution U_{ac} at the bell, which is added to the outgoing flow rate of the trombone U_{tb} , so that the total flow rate is equal to $U_{tb} + U_{ac}$ on the spherical isobar where the microphone is placed. As a consequence, this spherical isobar can be seen as a junction linking the two systems {Trombone Resonator} and {Controller}, which are fed by the same input, and whose outputs add up to each other.

For sake of simplicity, the microphone is described as a linear pressure-to-voltage converter with unit gain. The

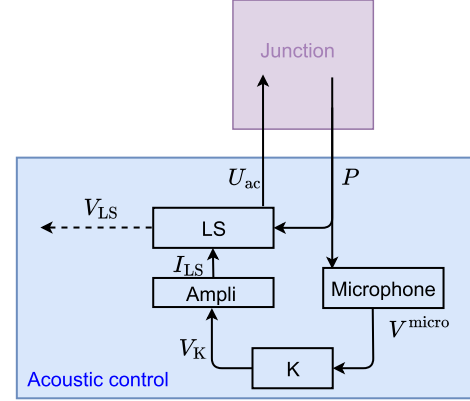


Figure 3. Block diagram in the Laplace domain of the overall control structure. It is composed of a microphone (transfer function between acoustic pressure P and voltage V^{micro}), a controller (cascaded transfer functions K and $Ampli$ between voltage V^{micro} and current I_{LS} and a loudspeaker LS (quadripole with two inputs – pressure P and current I_{LS} – and two outputs – voltage V_{LS} and flow rate U_{ac}).

loudspeaker behaves like an electrical current to acoustic flow converter. Thus, between these two transducers, the controller designed to impose the desired vocal tract transfer function between U_{tb} and U_R , must convert a voltage into a current. For later experimental implementation, the controller transfer function is separated into two cascaded parts:

- the one, called *Ampli* in Figure 3, converts a voltage into a current with unit gain. An electronic solution of design has been proposed by Mc Pherson, based on a feedback loop circuit including an operational amplifier [23].
- the other, called *K*, which must therefore supply an electrical voltage, can thus be implemented in a conventional digital signal processor. Its expression is derived in Section 5.

2.5 Summary

In summary, this paper proposes the design of an active control system, localised at the bell, that operates as a targetable mute. Note that, as standard mutes do, such control impacts the entire instrument and the acoustic boundary conditions experienced by the musician's lips (the input impedance in the linear time-invariant case of a static bore at low amplitude levels). In this context, the active control is not merely an electronic vocoder effect played back through external loudspeakers.

3 Radiation impedance Z_R and vocal tract H_{VT} modeling

This section presents models of the components required for calculating the acoustic control law (transfer function K). These models refer to the components of

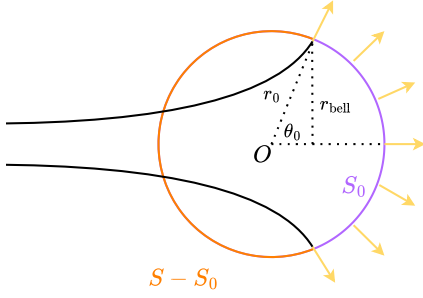


Figure 4. Radiation model of the bell of a wind instrument. The purple spherical cap S_0 is the uniformly animated part and the orange cap $S - S_0$ is motionless (see details in [26]).

Block B presented in Figure 2 (see Sect. 2.2): the radiation impedance Z_R (in Sect. 3.1) and the vocal tract transfer function H_{VT} (in Sect. 3.2). A particular attention is paid to the choice of its modelling, which results from a compromise between realism (consideration of non-planar wavefronts) and simplicity.

3.1 Radiation

Several acoustic radiation models are available (see e.g., [24, 25] for a review of classical models) for the 1D modelling of musical instruments. A first interest of the work proposed in [26] is to account for the effect of isobar curvature at the bell outlet, by assuming that the bell radiates similarly to a pulsating spherical cap (see Fig. 4). A second interest is to approximate the impedance formula (decomposed over spherical harmonics) with optimised simpler differential models. The model chosen here is the second-order high-pass filter described below, which exhibits better results than classical 1D planar models (see [27, 28]).

This radiation impedance $Z_R = \frac{P_{\text{out}}}{U_{\text{out}}}$ is modelled in the Laplace domain by

$$Z_R(s) = \frac{\rho_0 c_0}{S_0} \tilde{Z} \left(\frac{s}{\omega_0} \right) \quad \text{with} \quad \omega_0 = \frac{2\pi c_0 \nu_c(\theta_0)}{r_0}, \quad (2a)$$

$$\tilde{Z}(\tilde{s}) = \frac{\alpha(\theta_0) \tilde{s} + \tilde{s}^2}{1 + 2\xi(\theta_0) \tilde{s} + \tilde{s}^2} \quad (\text{adimensioned}), \quad (2b)$$

where (see Tab. 1) ρ_0 and c_0 are the air density and the speed of sound, r_0 is the sphere radius, θ_0 is the cap half-angle ($r_0 = \frac{r_{\text{bell}}}{\sin(\theta_0)}$), and where optimal parameters α , ξ and ν_c are given by the following functions, defined for all $\theta_0 \in [0, \frac{\pi}{2}]$, $\xi(\theta_0) = 0.0207\theta_0^4 - 0.144\theta_0^3 + 0.221\theta_0^2 + 0.0799\theta_0 + 0.72 \geq 0$, $\alpha(\theta_0) = (0.1113\theta_0^5 - 0.636\theta_0^4 + 1.162\theta_0^3 - 1.242\theta_0^2 + 1.083\theta_0 + 0.8788)^{-1} \geq 0$ and $\nu_c(\theta_0) = (-0.198\theta_0^5 + 0.2607\theta_0^4 - 0.424\theta_0^3 - 0.07946\theta_0^2 + 4.704\theta_0 + 0.022)^{-1} \geq 0$.

The Laplace region of convergence of Z_R includes \mathbb{C}_0^+ (denoting $\mathbb{C}_0^+ = \{s \in \mathbb{C} \text{ s.t. } \Re(s) > 0\}$) and it is proved to define a causal, stable, passive system [26, 28] which therefore meets the expectations formulated in

Table 1. Numerical values of parameters used in the model of Z_R . r_{bell} is measured on a trombone *Jupiter JVL 528*. The value of θ_0 comes from [26].

Symbol	Value	Unit
ρ_0	1.2	kg.m ⁻³
c_0	340	m.s ⁻¹
r_{bell}	$8.0 \cdot 10^{-2}$	m
θ_0	72.4	°
$r_0 = \frac{r_{\text{bell}}}{\sin(\theta_0)}$	$8.39 \cdot 10^{-2}$	m
$S_0 = 2\pi r_0^2(1 - \cos(\theta_0))$	$3.09 \cdot 10^{-2}$	m ²
f_c	893	Hz

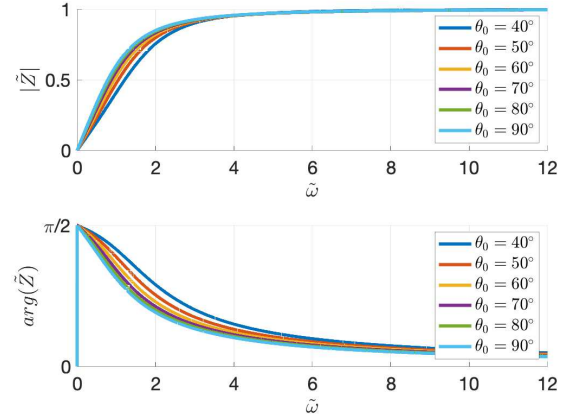


Figure 5. Bode diagram of adimensioned radiation impedance $\tilde{\omega} \mapsto \tilde{Z}(i\tilde{\omega})$. Note that the adimensioned angular frequency is $\tilde{\omega} = \omega/\omega_0 = 2\pi f/\omega_0$.

(H1), Section 2.3. Figure 5 shows the values of module and phase of \tilde{Z} for several values of θ_0 .

Note that the cutoff frequency (for which $|\tilde{Z}|^2 = \frac{1}{2}$) is given by $f_c = \frac{c_0}{r_0} \nu_c [[1 + \beta^2]^{\frac{1}{2}} - \beta]^{\frac{1}{2}}$ with $\beta = 1 + \alpha^2 - 2\xi^2$. For typical values measured on a real trombone bell, $\theta_0 = 72.4^\circ$ and $r_0 = 8.39$ cm, f_c is equal to 893 Hz.

3.2 Vocal tract

To design the vocal effect subsequently applied by active control to the radiated impedance of the trombone, we consider a static vocal tract (producing one vowel, see (H2)). Then, we need a model of its flow-to-flow filter (see (1)), the resonances of which are related to formants and characterise the vowel. This linear time-invariant causal filter is derived by considering N_{VT} cascaded straight pipes of equal length and of cross-section area a_n (see Fig. 6), radiating in a semi-infinite end pipe of cross-section area a_{ext} . As proposed by Mathur et al. [29], their length, equal to 3.968 mm, is slightly greater than the distance covered in half a sampling period. This allows the vocal tract to vary in length and leads to a more realistic synthesis. This filter admits a standard Kelly-Lochbaum structure [30, 31] with relevant computational

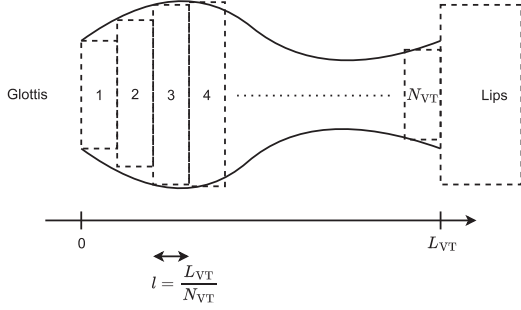


Figure 6. Modelling the vocal tract.

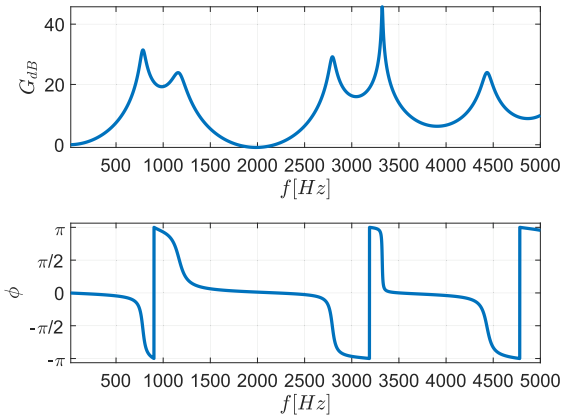


Figure 7. Bode diagram of the transfer function $H_{VT}(s = 2i\pi f)$ of a vocal tract for the vowel profile [a] (see Fig. 8), loaded by $Z_R^{VT} = \rho_0 c_0 / a_{ext}$ with $a_{ext} = 38.2 \text{ cm}^2$: (top) modulus in dB; (bottom) phase in radians.

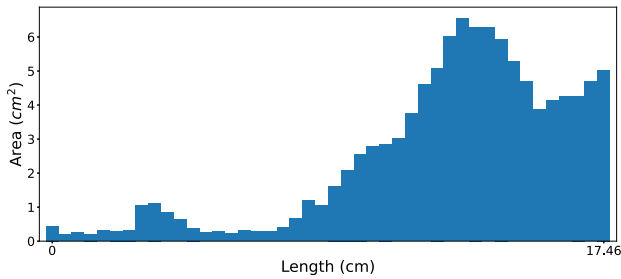


Figure 8. Area profile of the vocal tract for vowel [a] extracted from [31, Table 3] ($N_{VT} = 44$ cascaded pipes, total length $L_{VT} = 17.46 \text{ cm}$, so that $L_{VT}/N_{VT} = 3.968 \text{ mm}$).

details provided in Appendix D to ensure self-consistency (see Fig. D.1 and Eqs. (D.1), (D.2)).

The vocal tract transfer function $H_{VT} = U_{out}/U_{in}$ is derived from the transfer matrix T_{VT} of the cascaded pipes loaded by a radiation impedance Z_R^{VT} , so that

$$\begin{bmatrix} P_{in} \\ U_{in} \end{bmatrix} = \underbrace{T_{VT} \begin{bmatrix} Z_R^{VT} \\ 1 \end{bmatrix}}_{\begin{bmatrix} * \\ H_{VT}^{-1} \end{bmatrix}} U_{out}. \quad (3)$$

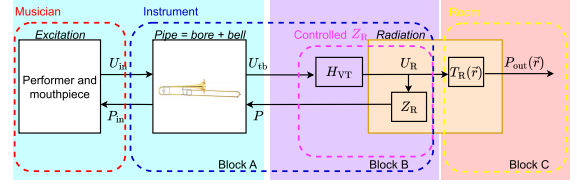


Figure 9. Block diagram of the target radiation impedance in the Laplace domain. Here, the vocal tract H_{VT} is placed between the pipe and the radiation such that the new radiation flow rate U_R is now equal to $U_R = H_{VT}U_{tb}$.

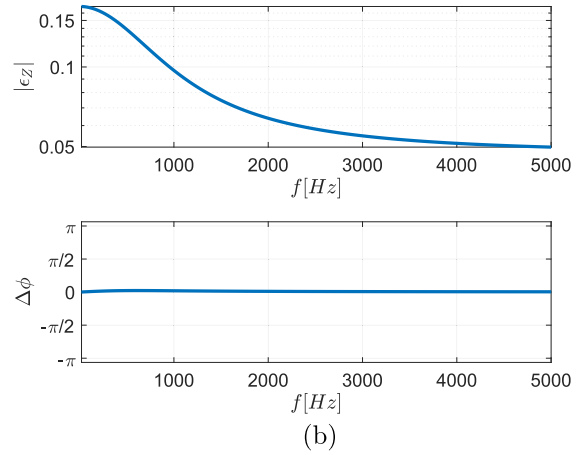
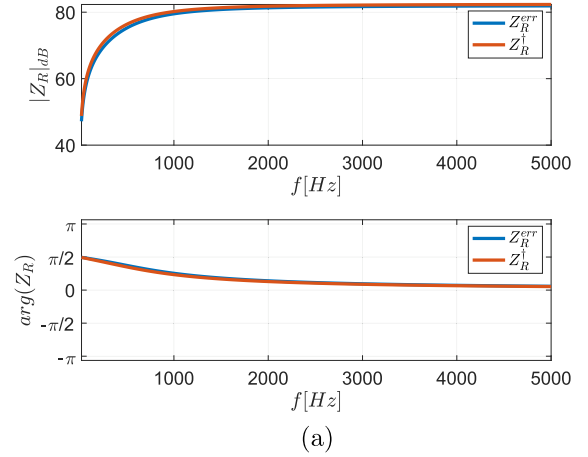


Figure 10. Bode diagrams: (a) radiation impedances Z_R^\dagger (exact, in red) corresponding to $\theta_0^\dagger = 72.4^\circ$ and Z_R^{err} (erroneous, in blue) corresponding to $\theta_0^{err} = 76.02^\circ$ (deviation of 5%); (b) error characterisation. (a) radiation impedances: (bottom) phase in radians. (b) error: (top) relative error modulus $|\epsilon_Z|$ (log scale); (bottom) phase deviation $\Delta\phi = \phi^{err} - \phi^\dagger$.

Figure 7 shows the Bode diagram of H_{VT} computed for the vowel [a] described by the area profile in Figure 8 and choosing¹ $a_{ext} = 38.2 \text{ cm}^2$.

¹ This corresponds to a typical quality factor $Q = 10$ for the first resonance of a straight pipe with the cross-section area 3 cm^2 (approximate averaged value of cross-section area based on Fig. 8).

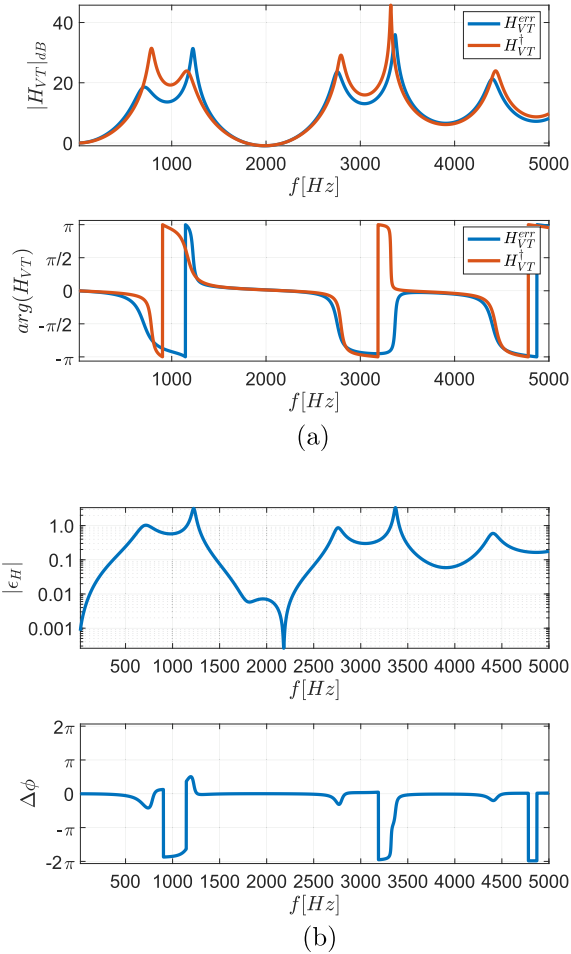


Figure 11. Bode diagrams: (a) vocal tract filters H^\dagger (exact, in red) and H^{err} (erroneous, in blue); (b) error characterisation. (a) vocal tract filters: (top) modulus in dB; (bottom) phase in radians. (b) error: (top) relative error modulus $|\epsilon_H|$ (log scale); (bottom) phase deviation $\Delta\phi = \phi^{\text{err}} - \phi^\dagger$.

4 Target acoustic control

This section introduces the control law designed within the acoustic domain to achieve the desired behaviour. This law relies solely on the radiation impedance Z_R and the transfer function H_{VT} of the target vowel². Subsequently, the robustness of vowel rendering is evaluated. Initially, a basic test examines deviations due to an angle error θ_0 in the radiation impedance model. Following this, a sensitivity analysis with respect to θ_0 and temperature T is presented.

4.1 Control model

As mentioned in Section 1, the target application is to produce a vocalised version of the radiated sound. This amounts to applying resonances (through H_{VT}) to the

² This means that the law is independent of the trombone configuration and the played note, but it is valid only for a static vowel.

Table 2. Comparison of the frequencies F_k and amplitudes A_k of the first five peaks of H^\dagger and H^{err} .

k	1	2	3	4	5
F_k^\dagger [Hz]	785	1158	2795	3323	4434
A_k^\dagger [dB]	31.4	24.0	29.2	45.8	23.9
F_k^{err} [Hz]	710	1224	2775	3369	4400
A_k^{err} [dB]	18.6	31.4	23.7	36.0	21.2
$\frac{F_k^{\text{err}} - F_k^\dagger}{F_k^\dagger}$	-9.6%	+5.7%	-0.7%	+1.4%	-0.8%
$\frac{A_k^{\text{err}} - A_k^\dagger}{A_k^\dagger}$	-77%	+134%	-46%	-67.6%	-26.7%

Table 3. Numerical values of physical parameters. The value of θ_0^\dagger is taken from [26].

Symbol	Value	Unit
γ	7/5	\emptyset
R	8.314	$\text{J.K}^{-1}.\text{mol}^{-1}$
M	29	g.mol^{-1}
P_0	1	bar
θ_0^\dagger	72.4	$^\circ$
T^\dagger	300	K

radiated pressure (originally generated by the trombone flow rate U_{tb}). To this end, the principle consists of adding a controlled acoustic flow rate (U_{ac}) to that of the trombone (U_{tb}) at the bell extremity in order to form a modified version of the flow rate ($U_{\text{R}} = U_{\text{tb}} + U_{\text{ac}}$) experienced by the natural acoustic radiation. This is implemented by adding a flow source, assumed to be ideal in the low frequency range (H1), so that it defines an ideal conservative junction with three ports, that balances flows and equalises pressures (see Fig. 2), that is,

$$U_{\text{tb}} + U_{\text{ac}} = U_{\text{R}}, \quad (4a)$$

$$P_{\text{tb}} = P_{\text{ac}} = P_{\text{R}} \quad (:= P). \quad (4b)$$

Then, the control is designed such that the flow experienced by the radiation (U_{R}) becomes a vocalised version of the trombone flow ($H_{VT}U_{\text{tb}}$) rather than the trombone flow itself (U_{tb}), that is (see Fig. 9)

$$U_{\text{R}} = H_{VT}U_{\text{tb}}. \quad (5)$$

Note that, from the trombone viewpoint, this amounts to loading its bell extremity by the modified radiation impedance $H_{VT}Z_{\text{R}}$, denoted Z_{R}^c below.

Then, modelling the acoustic control by its admittance $Y_{\text{ac}} = U_{\text{ac}}/P_{\text{ac}}$, it follows from (4a) that, at the acoustic junction,

$$U_{\text{tb}} + Y_{\text{ac}}P_{\text{ac}} = Z_{\text{R}}^{-1}P_{\text{R}}. \quad (6a)$$

The expected target ($U_{\text{R}} = H_{VT}U_{\text{tb}}$) is achieved if $U_{\text{tb}} = H_{VT}^{-1}U_{\text{R}} = H_{VT}^{-1}Z_{\text{R}}^{-1}P_{\text{R}}$, so that (6a) becomes

$$H_{VT}^{-1}Z_{\text{R}}^{-1}P_{\text{R}} + Y_{\text{ac}}P_{\text{ac}} = Z_{\text{R}}^{-1}P_{\text{R}}. \quad (6b)$$

Finally, from (4b), the target acoustic control admittance is

$$Y_{ac} = (1 - 1/H_{VT})/Z_R, \quad (7a)$$

leading to the equivalent formula for the vocal tract filter

$$H_{VT} = (1 - Z_R Y_{ac})^{-1}. \quad (7b)$$

4.2 Qualitative robustness test

Denote H_{VT}^\dagger the target vocal filter. Denote Z_R^\dagger the exact (but unknown) radiation impedance and Z_R^{err} the (possibly) erroneous model.

Following (7a), the acoustic control we compute for H_{VT}^\dagger and Z_R^{err} leads to $Y_{ac}^{\text{err}} = (1 - 1/H_{VT}^\dagger)/Z_R^{\text{err}}$. Using this control Y_{ac}^{err} , the vocal filter produced in reality by the exact radiation Z_R^\dagger is, following (7b) $H_{VT}^{\text{err}} = (1 - Z_R^\dagger Y_{ac}^{\text{err}})^{-1}$, that is

$$H_{VT}^{\text{err}} = \frac{1}{1 - (Z_R^\dagger/Z_R^{\text{err}})(1 - 1/H_{VT}^\dagger)}. \quad (8)$$

Following this equation, the relative errors

$$\epsilon_H := \frac{H_{VT}^{\text{err}} - H_{VT}^\dagger}{H_{VT}^\dagger} \quad \text{and} \quad \epsilon_Z := \frac{Z_R^{\text{err}} - Z_R^\dagger}{Z_R^\dagger}, \quad (9a)$$

committed respectively on the vocal filter and on the radiation impedance, are related by

$$\epsilon_H = \epsilon_Z \frac{1 - H_{VT}^\dagger}{1 + \epsilon_Z H_{VT}^\dagger}. \quad (9b)$$

A robustness test is presented for H_{VT}^\dagger given in Figure 7 where Z_R^\dagger , with parameter $\theta_0^\dagger = 72.4^\circ$ (see (2a), (2b) and Tab. 1), is erroneously replaced by Z_R^{err} , with the same parameters except a deviation of +5% on the angle $\theta_0^{\text{err}} = 1.05 \theta_0^\dagger \approx 76.02^\circ$ (see Fig. 10).

The vocal tract filter H_{VT}^{err} resulting from (8) is compared to H_{VT}^\dagger in Figure 11: the peaks are modified (see Tab. 2) but are still qualitatively representative of a vowel [a]. In the following section, we complete this test by a sensitivity analysis.

4.3 Sensitivity analysis

In this section, we analyse the sensitivity of H_{VT} to the parameters $\mathbf{a} = (T, \theta_0)$, assuming that:

- (i) a target control Y_{ac}^\dagger is pre-computed from (7a) with fixed parameters $T^\dagger = 300 \text{ K}$, $\theta_0^\dagger = 72.4^\circ$,
- (ii) the radiation impedance is subject to small variations in its parameters \mathbf{a} around $\mathbf{a}^\dagger = (T^\dagger, \theta_0^\dagger)$, and is denoted $Z_R(s; \mathbf{a})$.

In this case, the dependency of the vocal tract filter to parameters \mathbf{a} reads, from (7b),

$$H_{VT}(s; \mathbf{a}) = (1 - Z_R(s; \mathbf{a})Y_{ac}^\dagger)^{-1}. \quad (10a)$$

Then, the first order expansion of $H_{VT}(s; \mathbf{a}^\dagger + \delta \mathbf{a})$ with respect to $\delta a_1 = \delta T$ and $\delta a_2 = \delta \theta_0$ leads to

$$H_{VT} = H_{VT}^\dagger + S_T \delta T + S_{\theta_0} \delta \theta_0 + \mathcal{O}(\delta T^2 + \delta \theta_0^2), \quad (10b)$$

introducing $H_{VT}^\dagger(s) = H_{VT}(s; \mathbf{a}^\dagger)$ and the sensitivity functions for $a_1 = T$ and $a_2 = \theta_0$ as

$$S_{a_i}(s; \mathbf{a}) = \frac{\partial H_{VT}(s; \mathbf{a})}{\partial a_i}. \quad (10c)$$

From (10a), it follows that

$$S_{a_i} = \frac{Y_{ac}^\dagger}{(1 - Y_{ac}^\dagger Z_R)^\dagger} \frac{\partial Z_R}{\partial a_i}, \quad (11a)$$

where $\frac{\partial Z_R}{\partial a_i}$ is derived from the chain rule applied to (2a), (2b) in which ρ_0 , c_0 , S_0 , ω_0 are the \mathbf{a} -dependent functions

$$\rho_0(T) = \frac{P_0 M}{RT}, \quad (12a)$$

$$c_0(T) = \sqrt{\frac{\gamma RT}{M}}, \quad (12b)$$

$$S_0(\theta_0) = 2\pi \left(\frac{r_{\text{bell}}}{\sin(\theta_0)} \right)^2 (1 - \cos(\theta_0)), \quad (12c)$$

$$\omega_0(\theta_0) = \frac{2\pi c_0(T) \nu_c(\theta_0)}{r_0(\theta_0)}, \quad \text{with } r_0(\theta_0) = \frac{r_{\text{bell}}}{\sin(\theta_0)}, \quad (12d)$$

and $\alpha(\theta_0)$, $\xi(\theta_0)$ and $\nu_c(\theta_0)$ are detailed in Section 3.1.

The physical values of parameters are given in Table 3.

Note that detailing the expression of the sensitivity functions of the characteristic impedance

$$Z_c(T, \theta_0) = \frac{\rho_0(T)c_0(T)}{S_0(\theta_0)} = \sqrt{\frac{\gamma M}{RT}} \frac{P_0}{\pi r_{\text{bell}}^2} \cos^2\left(\frac{\theta_0}{2}\right) \quad (13)$$

involved in (2a) yields

$$\frac{\partial Z_c}{\partial \theta_0} = -\sqrt{\frac{\gamma M}{RT}} \frac{P_0}{2\pi r_{\text{bell}}^2} \sin(\theta_0), \quad (14a)$$

$$\text{and } \frac{\partial Z_c}{\partial T} = -\sqrt{\frac{\gamma M}{RT^3}} \frac{P_0}{2\pi r_{\text{bell}}^2} \cos^2\left(\frac{\theta_0}{2}\right). \quad (14b)$$

Figure 12 reveals that variations in θ_0 and T have a significant impact on the position and amplitude of vocal tract resonances, potentially modifying the radiated vowel. In particular, overestimation of θ_0 tends to separate resonances 1 & 2 on the one hand, and 3 & 4 on the other, and to reduce the 5th resonance frequency. Underestimation of θ_0 has the opposite effect, fusing resonances 1 & 2 when $\theta_0 = 80^\circ$. Estimation errors on T cause resonance

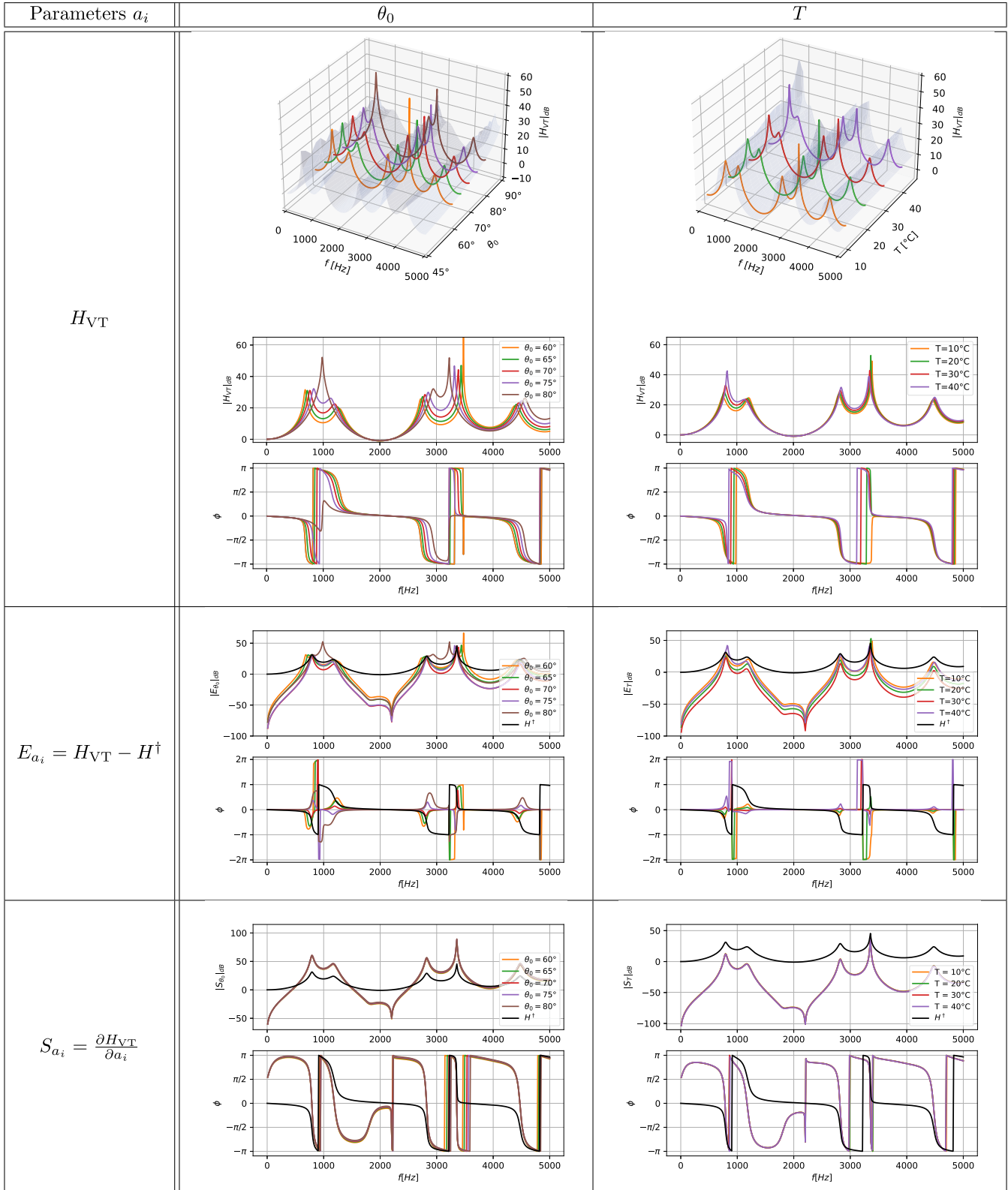


Figure 12. Bode diagram (modulus and phase) of the vocal tract filter H_{VT} . The variation in the value of the a_i parameters is studied in order to observe the changes in the transfer function. The errors E_{a_i} and sensitivities S_{a_i} are presented for several variations of a_i .

Table 4. Physical, Thiele and Small and reduced parameters of the speaker SICA 3L 0.8 SL 8Ω mode Z000900, given by the manufacturer. *Note:* Greyed-out parameters in the first 2 lines are not used in the expression of the controller K , because it is designed to control the loudspeaker in current.

	Physical parameters		Reduced parameters	
	Symbol	Value	Symbol	Value
Electrical	R_e	8Ω	$\tau_e = \frac{L_e}{R_e}$	1.38 · 10 ⁻⁵ s
	L_e	0.11 mH	$\beta_e = \frac{1}{L_e}$	9.09 · 10 ³ H ⁻¹
Electro/Mechanical Coupling	$Bl = 2.8 \text{ N} \cdot \text{A}^{-1}$			
Mechanical	C_{ms}	602 μm.N ⁻¹	$\beta_m = \frac{1}{M_{ms}}$	5.26 · 10 ² kg ⁻¹
	R_{ms}	4.06 · 10 ⁻¹ N.m ⁻¹ .s	$\tau_m = \frac{M_{ms}}{R_{ms}}$	4.68 · 10 ⁻³ s
	M_{ms}	1.9 · 10 ⁻³ kg	$\omega_m = \frac{1}{\sqrt{C_{ms}M_{ms}}}$	9.35 · 10 ² rad.s ⁻¹
Mechanical/Acoustic Coupling	$S_d = 30.2 \text{ cm}^2$			

frequencies to move in the same direction as estimation errors on θ_0 , but to a lesser extent, at usual temperatures. Indeed, previous measurements carried out with real players [32] show that the temperature in the bore generally rises while playing from room temperature to around 37.7°C, the temperature of the human body, inducing typical variations of the order of 10°C. Consequently, an incorrect temperature estimate should have a negligible effect on the vocal tract resonances applied to the radiated sound.

5 Electro-acoustic implementation

The active control solution implemented uses a loudspeaker at the end of the bell as an actuator. Section 5.1 presents a brief reminder on its standard linear electro-acoustic modelling with Thiele and Small parameters [33, 34]. In this paper the loudspeaker is driven by a current source assumed to be ideal on the frequency range of interest. Note that the natural causal electric input of a loudspeaker is the voltage (and not the current). This means that the current source requires the use of a dedicated feedback-loop circuit involving an operational amplifier (see e.g., [23]). The output current (see Fig. 3) is governed by $I_{LS} = K V^{\text{micro}}$ where $V^{\text{micro}} = K_{\text{mic}} P$ denotes the voltage delivered by a pressure microphone of ideal gain K_{mic} . The pressure-to-current gain is then described by $I_{LS} = K_{\text{tot}} P$ with $K_{\text{tot}} = K \cdot K_{\text{mic}}$.

The transfer function K_{tot} is the electronic control to be determined in Section 5.2, in order to realise the acoustic target Y_{ac} given the loudspeaker model.

5.1 Loudspeaker modelling

A basic linear description of the loudspeaker (LS) is modelled by the following electrical and mechanical equations, cf. [33, 34]:

$$v_{LS}(t) = R_e i_{LS}(t) + L_e \frac{di_{LS}}{dt} + Bl \frac{dz}{dt}, \quad (15a)$$

$$M_{ms} \frac{d^2z}{dt^2} = Bl i_{LS}(t) - R_{ms} \frac{dz}{dt} - \frac{1}{C_{ms}} z(t) - S_d P, \quad (15b)$$

where M_{ms} is the mass of the driver diaphragm and voice-coil assembly, R_{ms} and C_{ms} the mechanical resistance and compliance (suspension, spider, acoustic chamber) and S_d the equivalent surface area of the cone. Bl is the coefficient of the magnetic force induced by the current passing through the voice-coil of length l . This model admits the following input (u)–state (x)–output (y) representation:

$$\dot{x} = Ax + Bu, \quad y = Cx, \quad (16a)$$

$$\text{with } u = \begin{bmatrix} v_{LS} \\ P \end{bmatrix}, \quad x = \begin{bmatrix} i_{LS} \\ z \\ \dot{z} \end{bmatrix}, \quad y = \begin{bmatrix} i_{LS} \\ U_{LS} \end{bmatrix}, \quad (16b)$$

$$A = \begin{bmatrix} -\frac{1}{\tau_e} & 0 & -Bl\beta_e \\ 0 & 0 & 1 \\ Bl\beta_m & -\omega_m^2 & -\frac{1}{\tau_m} \end{bmatrix}, \quad B = \begin{bmatrix} \beta_e & 0 \\ 0 & 0 \\ 0 & -S_d\beta_m \end{bmatrix}, \quad (16c)$$

$$C = \begin{bmatrix} 1 & 0 & 0 \\ 0 & 0 & S_d \end{bmatrix}. \quad (16d)$$

Parameters used for simulations are given in Table 4.

5.2 Controller expression

The state-space representation recalled in Section 5.1 describes a causal stable system. However, as mentioned above, we consider here that the loudspeaker is controlled by a current source (I_{LS}). In this case, expressing the position $Z(s)$ as $U_{LS}(s)/(S_d \cdot s)$ in the Laplace domain (for zero initial conditions), it straightforwardly follows from (15b) that

$$U_{LS}(s) = A_I(s) I_{LS}(s) + A_P(s) P(s), \quad (17a)$$

$$\begin{aligned} A_I(s) &= \frac{s S_d Bl}{M_{ms} s^2 + R_{ms} s + \frac{1}{C_{ms}}} \\ &= \frac{S_d Bl \beta_m s}{s^2 + \frac{s}{\tau_m} + \omega_m^2}, \end{aligned} \quad (17b)$$

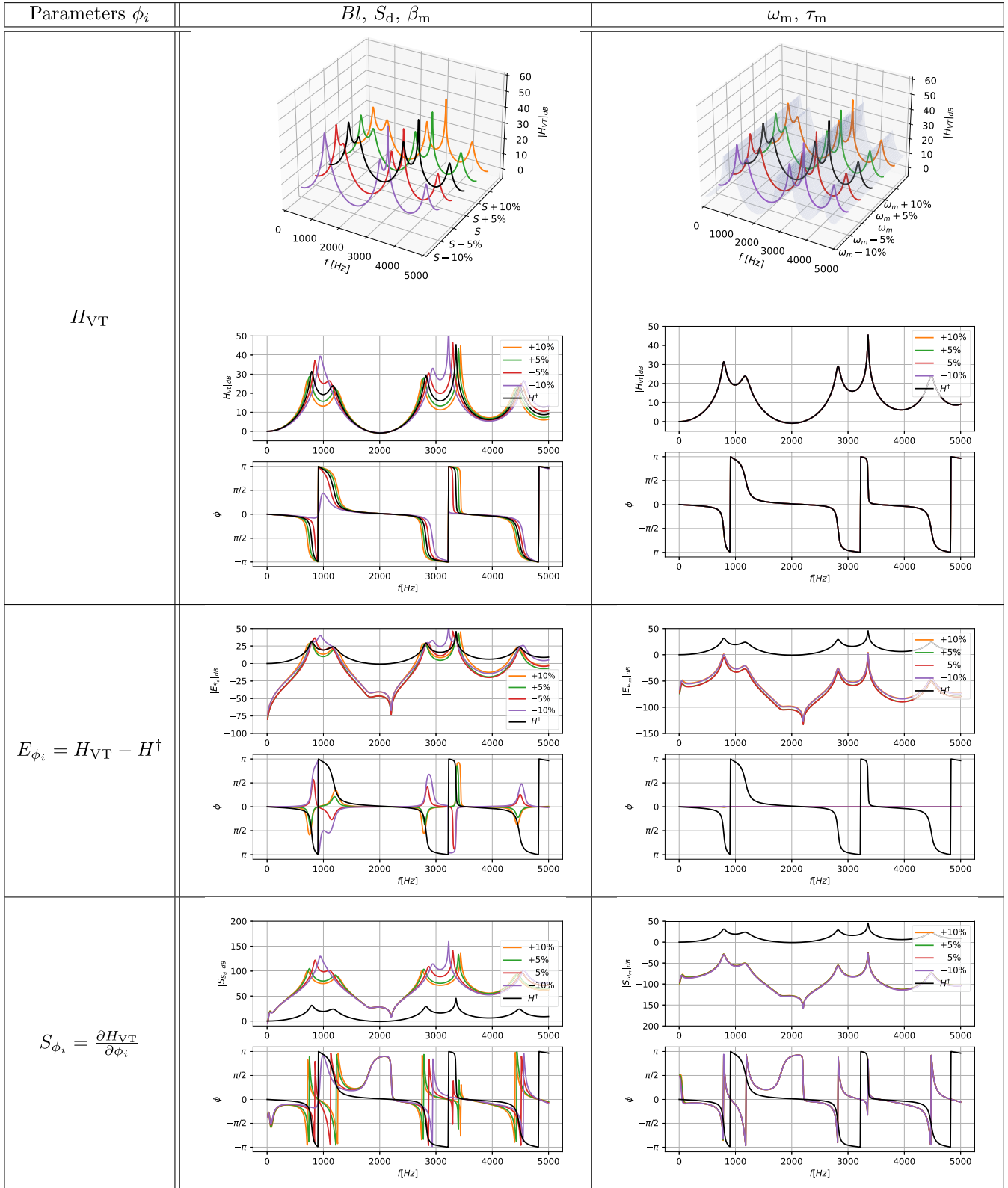


Figure 13. Bode diagram (modulus and phase) of the vocal tract H_{VT} . The variation in the value of the ϕ_i parameters is studied in order to observe the changes in the transfer function. The errors E_{ϕ_i} and sensitivities S_{ϕ_i} are also presented for variations of ϕ_i between -10% and $+10\%$. The variations in Bl , S_d and β_m (left-hand column) considerably impact the amplitudes and positions of the formants. In contrast, variations in ω_m and τ_m (right-hand column) have negligible effect on H_{VT} .

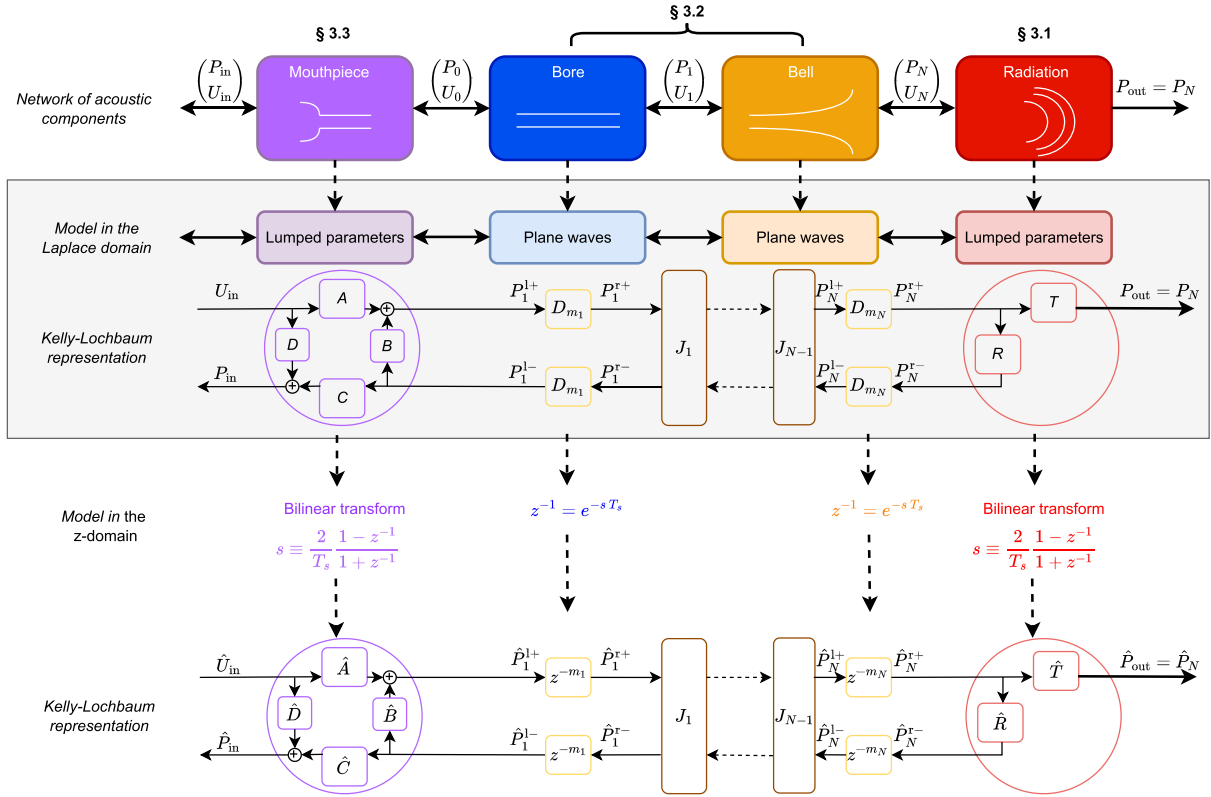


Figure 14. Description of the numerical testbed use for the trombone in the continuous and discrete time. Transfer functions A , B , C , D , T and R are given in equations X , from which transfer functions \hat{A} , \hat{B} , \hat{C} and \hat{D} , \hat{T} and \hat{R} are deduced using the bilinear transform: $\forall z \in \mathbb{C} \text{ s.t. } |z| < 1, s = 2f_s \frac{1-z^{-1}}{1+z^{-1}}$, and given in equations (23a)–(23f), using $\kappa = \frac{\tau_0}{2\pi\nu_c(\theta_0) c_0}$.

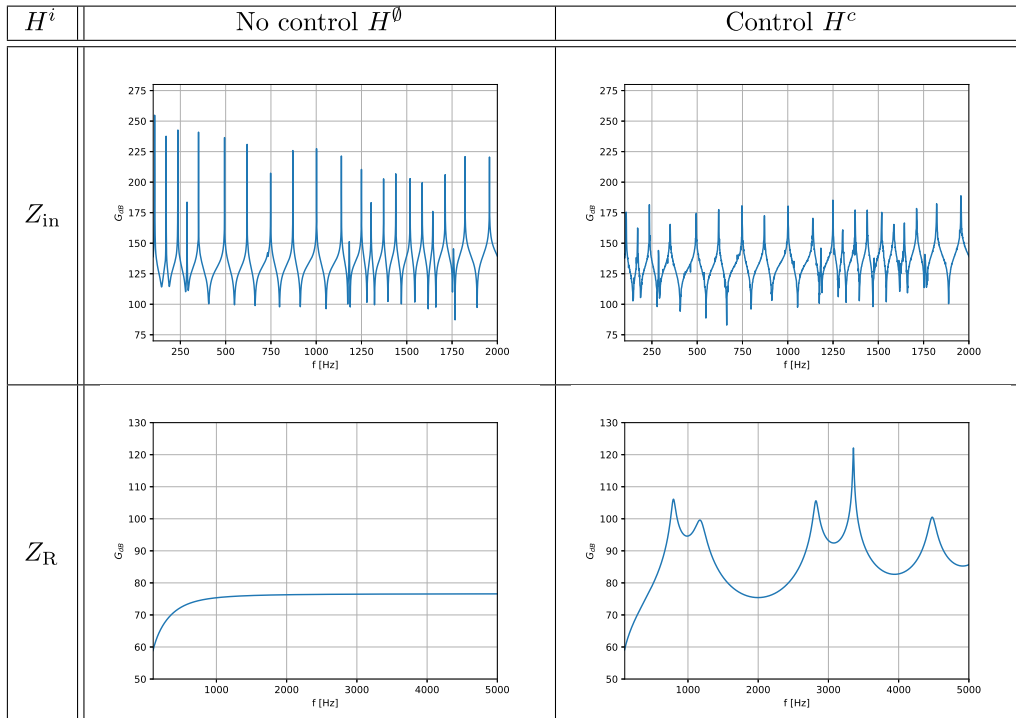


Figure 15. Transfer functions $H^i = Z_{in}, Z_R$ in the Fourier domain, with ($i = c$) control and without ($i = \emptyset$) control. The amplitude differences and frequency deviations of resonance peaks are noted in Table 5.

Table 5. Comparison of the first five frequencies peaks F_k and amplitudes A_k of the first five peaks of the input impedance without control Z_{in}^0 and with control Z_{in}^c .

k	1	2	3	4	5
F_k^0 [Hz]	109	173	237	288	351
A_k^0 [dB]	192	177	178	139	164
F_k^c [Hz]	108	172	234	287	349
A_k^c [dB]	183	159	170	145	163
$\frac{F_k^c - F_k^0}{F_k^0}$	-0.91%	-0.58%	-1.12%	-0.34%	-0.56%

$$\begin{aligned} A_P(s) &= \frac{-s S_d^2}{M_{\text{ms}} s^2 + R_{\text{ms}} s + \frac{1}{C_{\text{ms}}}} \\ &= \frac{-s S_d^2 \beta_m}{s^2 + \frac{s}{\tau_m} + \omega_m^2}. \end{aligned} \quad (17c)$$

In practice, the current generator is built according to the Howland model [23]. Here, we consider that its cut-off frequency is higher than the frequency range of interest. As a result, the chain composed of the microphone, the current source and the amplifier is a constant gain arbitrarily set at 1 to simplify the following calculations. Then, the transfer function from P to I_{LS} , shown in Figure 3, is equal to K . It follows from (17a) that:

$$U_{\text{LS}} = (A_I K + A_P) P. \quad (18)$$

Finally, from (4a) with $U_{\text{ac}} = U_{\text{LS}}$, the radiated flow is given by $U_{\text{R}} = U_{\text{tb}} + (A_I K + A_P) Z_{\text{R}} U_{\text{R}}$, so that by identification with (5), the controller transfer function is:

$$K = A_I^{-1} \left[\frac{1}{Z_{\text{R}}} (1 - H_{\text{VT}}^{-1}) - A_P \right]. \quad (19)$$

Passivity of the controller

According to hypothesis (H3) (cf. Sect. 2.3) and to the properties of Z_{R} (cf. Sect. 3.1), K is passive as a multiplication of passive elements.

5.3 Sensitivity to the Thiele and Small parameters

In the same way as in Section 4.3, we study the controller sensitivity to the following five reduced parameters noted ϕ_i : Bl , ω_m , τ_m , β_m , S_d . From (19) it follows that:

$$H_{\text{VT}} = [1 - Z_{\text{R}}(A_I K + A_P)]^{-1}, \quad (20)$$

in which H_{VT} , A_I and A_P depend on ϕ_i . Note that Z_{R} is independent of the loudspeaker and K is assumed to be fixed.

We use the chain rule on (20) to obtain several functions of sensitivity:

$$\frac{\partial H_{\text{VT}}}{\partial \phi_i} = S_{\phi_i}$$

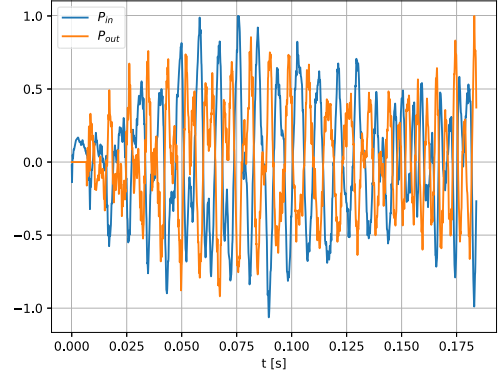


Figure 16. Normalized acoustic pressure waveforms in the trombone mouthpiece \hat{P}_{in} and at the bell \hat{P}_{out} , simulated from a measurement of acoustic flowrate in a real trombone mouthpiece

$$= Z_{\text{R}} \left[\frac{\partial A_I}{\partial \phi_i} K + \frac{\partial A_P}{\partial \phi_i} \right] [1 - Z_{\text{R}}(A_I K + A_P)]^{-2}. \quad (21)$$

Then:

$$H_{\text{VT}} = H_{\text{VT}}^\dagger + \sum_i S_{\phi_i} \delta \phi_i + \sum_i \mathcal{O}(\delta \phi_i^2), \quad (22)$$

where the sensitivity functions S_{ϕ_i} are calculated from nine terms $\partial A_I / \partial \phi_i$, $\phi_i \in \{Bl, \beta_m, S_d, \omega_m, \tau_m\}$ and $\partial A_P / \partial \phi_i$, $\phi_i \in \{\beta_m, S_d, \omega_m, \tau_m\}$ (A_P does not depend on Bl). These terms can be grouped into two categories:

- the derivatives with respect to the parameters Bl , β_m , and S_d of the numerator, which are proportional to A_I and A_P :

$$\begin{aligned} \frac{\partial A_I}{\partial Bl} &= \frac{A_I}{Bl}, \\ \frac{\partial A_I}{\partial S_d} &= \frac{A_I}{S_d} \text{ and } \frac{\partial A_P}{\partial S_d} = \frac{2A_P}{S_d}, \\ \frac{\partial A}{\partial \beta_m} &= \frac{A}{\beta_m} \text{ with } A = A_i \text{ or } A_P \end{aligned}$$

- the derivatives with respect to the parameters ω_m and τ_m of the denominator, which multiply A_I and A_P by a low-pass filter and a band-pass filter respectively, of natural frequency equal to ω_m :

$$\begin{aligned} \frac{\partial A}{\partial \omega_m} &= -\frac{2\omega_m}{s^2 + \frac{s}{\tau_m} + \omega_m^2} A, \\ \frac{\partial A}{\partial \tau_m} &= \frac{s/\tau_m^2}{s^2 + \frac{s}{\tau_m} + \omega_m^2} A, \end{aligned}$$

with $A = A_I$ or A_P .

Figure 13 shows the vocal tract transfer functions calculated for different values of the loudspeaker parameters, their difference with the target vocal tract filter and the functions of sensitivity. It appears that the first category of parameters Bl , S_d and β_m , which has a strong impact on the derivatives of A_I and A_P , significantly modifies the

resonance amplitudes and frequencies of H_{VT} . Overestimating them by 10% even causes the first two formants to merge around 1 kHz, which affects the vowel produced. These parameters must therefore be determined experimentally as accurately as possible in order to build the desired target in the controller. In contrast, for the second category of parameters ω_m and τ_m , similar variations have negligible effect on the vocal tract transfer function.

6 Numerical experiments

In this section, we design a numerical testbed to test and examine the control of the trombone. Section 6.1 derives the numerical testbed. Section 6.2 presents the numerical experiments and discusses the results on the controller.

6.1 Numerical testbed

In the trombone modelling, we prioritise simplicity and ease of simulation in the discrete-time domain over incorporating the refinements (C1)–(C5) listed in Section 2.1, since the control law is independent of block A in Figure 2.

The trombone is decomposed into several passive components: a dissipative mouthpiece (described in Appendix A) and a trombone resonator composed of concatenated straight pipes (described in Appendix B). So that this approach yields a Kelly-Lochbaum structure like that used for the vocal tract system, because its passivity is preserved when it is discretized by bilinear transform.

All these steps are detailed in Appendix D and the full process is summarized in Figure 14.

$$\hat{A}(z) = \frac{1 + 2z^{-1} + z^{-2}}{[Y_0 + 2f_s C_a + 2f_s Y_0 R_a C_a + 4f_s^2 Y_0 C_a M_a] + z^{-1}[2Y_0 - 8Y_0 f_s^2 C_a M_a] + z^{-2}[Y_0 - 2f_s C_a - 2f_s Y_0 R_a C_a + 4Y_0 f_s^2 C_a M_a]} \quad (23a)$$

$$\hat{B}(z) = \frac{[Y_0 - 2f_s C_a + 2f_s Y_0 R_a C_a + 4f_s^2 Y_0 C_a M_a] + z^{-1}[2Y_0 - 8Y_0 f_s^2 C_a M_a] + z^{-2}[Y_0 + 2f_s C_a - 2f_s Y_0 R_a C_a + 4Y_0 f_s^2 C_a M_a]}{[Y_0 + 2f_s C_a + 2f_s Y_0 R_a C_a + 4f_s^2 Y_0 C_a M_a] + z^{-1}[2Y_0 - 8Y_0 f_s^2 C_a M_a] + z^{-2}[Y_0 - 2f_s C_a - 2f_s Y_0 R_a C_a + 4Y_0 f_s^2 C_a M_a]} \quad (23b)$$

$$\hat{C}(z) = \frac{2Y_0 + 4Y_0 z^{-1} + 2Y_0 z^{-2}}{[Y_0 + 2f_s C_a + 2f_s Y_0 R_a C_a + 4f_s^2 Y_0 C_a M_a] + z^{-1}[2Y_0 - 8Y_0 f_s^2 C_a M_a] + z^{-2}[Y_0 - 2f_s C_a - 2f_s Y_0 R_a C_a + 4Y_0 f_s^2 C_a M_a]} \quad (23c)$$

$$\hat{D}(z) = \frac{[1 + R_a Y_0 + 2f_s M_a Y_0] + z^{-1}[1 + 2R_a Y_0] + z^{-2}[1 + R_a Y_0 - 2f_s M_a Y_0]}{[Y_0 + 2f_s C_a + 2f_s Y_0 R_a C_a + 4f_s^2 Y_0 C_a M_a] + z^{-1}[2Y_0 - 8Y_0 f_s^2 C_a M_a] + z^{-2}[Y_0 - 2f_s C_a - 2f_s Y_0 R_a C_a + 4Y_0 f_s^2 C_a M_a]} \quad (23d)$$

$$\hat{R}(z) = \frac{[Z_c Y_2^c (2\alpha\kappa f_s + 4\kappa^2 f_s^2) - (1 + 4\xi\kappa f_s + 4\kappa^2 f_s^2)] + z^{-1}[-8\kappa^2 f_s^2 Z_c Y_2^c - (2 - 8\kappa^2 f_s^2)] + z^{-2}[Z_c Y_2^c (-2\alpha\kappa f_s + 4\kappa^2 f_s^2) - (1 - 4\xi\kappa f_s + 4\kappa^2 f_s^2)]}{[Z_c Y_2^c (2\alpha\kappa f_s + 4\kappa^2 f_s^2) + 1 + 4\xi\kappa f_s + 4\kappa^2 f_s^2] + z^{-1}[-8\kappa^2 f_s^2 Z_c Y_2^c + 2 - 8\kappa^2 f_s^2] + z^{-2}[Z_c Y_2^c (-2\alpha\kappa f_s + 4\kappa^2 f_s^2) + 1 - 4\xi\kappa f_s + 4\kappa^2 f_s^2]} \quad (23e)$$

$$\hat{T}(z) = Z_c \frac{[4\alpha Y_2^c \kappa f_s + 8Y_2^c \kappa^2 f_s^2] + z^{-1}[-16Y_2^c \kappa^2 f_s^2] + z^{-2}[-4\alpha Y_2^c \kappa f_s + 8Y_2^c \kappa^2 f_s^2]}{[Z_c Y_2^c (2\alpha\kappa f_s + 4\kappa^2 f_s^2) + 1 + 4\xi\kappa f_s + 4\kappa^2 f_s^2] + z^{-1}[-8\kappa^2 f_s^2 Z_c Y_2^c + 2 - 8\kappa^2 f_s^2] + z^{-2}[Z_c Y_2^c (-2\alpha\kappa f_s + 4\kappa^2 f_s^2) + 1 - 4\xi\kappa f_s + 4\kappa^2 f_s^2]} \quad (23f)$$

6.2 Numerical experiments on the controller: results and discussion

Two numerical experiments are implemented, aiming at simulating the model of trombone described in Section 3 in the absence and in the presence of the model of controller described in Section 4. The first experiment aims to validate the operation of the control structure proposed in this paper and the expression of the controller model given in (19). To this end, a swept sine covering the frequency range of interest and sampled at 44.1 kHz is synthesised and used as the discrete-time mouthpiece flow \hat{U}_{in} at the input of the trombone model. The outputs of the discrete-time model, namely the radiated pressure \hat{P}_{out} and the mouthpiece pressure \hat{P}_{in} are provided by the Kelly-Lochbaum representation of the trombone and the expressions \hat{A} , \hat{B} , \hat{C} , \hat{D} , \hat{R} and \hat{T} defined in Figure 14 and given by (23a)–(23e). The numerical scheme is detailed in Appendix E. The \hat{U}_{tbn} component of the discrete-time radiated flowrate at the bell is then approximated by $\frac{1}{Z_N}(P_N^r - P_N^r)$. In the presence of the controller, it is added to the \hat{U}_{ac} component provided by the loudspeaker. Finally, the radiation impedance and the input impedance are estimated by the ratios of the discrete Fourier Transforms $\hat{P}_{out}/\hat{U}_{tbn}$, and $\hat{P}_{in}/\hat{U}_{in}$ respectively. Figure 15 shows these ratios in the absence (left-hand column) and in the presence (right-hand column) of a controller.

In the absence of the controller (H^0): the estimate of Z_{in} is similar to the trombone input impedance given in (C.2) and shown in Figure C.1. In particular, the first 5 peaks corresponding to the 5 lowest notes played on the trombone with the slide in first position (excluding the pedal note) are superimposed (see Tabs. 5 and C.1). As exposed in Appendix C, the Z_{in} spectrum shows a decay of 20 dB per decade in the higher range, due to the mouthpiece acoustic compliance in parallel with the trombone resonator (see Appendix A). Then, the estimate of Z_R , (see Fig. 15), is also similar to the radiation impedance model described in Section 3.1 and shown in Figure 9.

In the presence of the controller (H^c): Z_{in} is slightly modified. As shown in Table 5, the first 5 resonance peaks are lowered in frequency, but by less than -1.12% , i.e. about one sixth of a semi-tone. The peak amplitudes are

also modified, particularly in the vicinity of the formant frequencies, i.e. where H_{VT} is large. Also, as expected, the spectral envelope of the radiation impedance Z_R is close to the multiplication $H_{VT}Z_R$. As a result, the presence of the controller has an effect on both the radiation and the input impedance of the trombone model. This means that the performer, while playing, should be able to feel the presence of the controller at the mouthpiece.

The second experiment aims to simulate the acoustic pressure in the mouthpiece and at the bell, in particular to listen to the controller effect on the sound of the trombone. For this purpose, the trombone model input is an acoustic flow waveform, extracted from previous measurements [35], with a duration of 184 ms and sampled at 44.1 kHz. The discrete-time acoustic pressure is calculated in the mouthpiece and at the bell using the Kelly-Lochbaum representation described in Figure D.1 in Appendix D. The vowel effect [a] applied to the trombone sound by active control can be appreciated by playing, listening and comparing the acoustic pressures P_{in} and P_{out} whose normalized waveforms are plotted in Figure 16. Their periods are similar, and approximately equal to 8.6 ms, which corresponds to a playing frequency of 116.28 Hz.

7 Conclusion

This analysis is a continuation of work begun previously [10]. By considering a simple but effective model of the instrument, the numerical results showed that it is possible to radiate a vowel through the trombone using active control. Sensitivity studies on the physical parameters and on the loudspeaker parameters allow us to envisage physical experiments.

Further studies will aim to develop a radiation-independent control, so that the control can be adapted to any playing situation. All the hypotheses cited above are discussed in perspective of an experimental realization: choice and co-location of microphones, pressure-to-voltage converter, loudspeakers.

The application of this work to a real trombone will be the object of a next publication.

Conflicts of interest

The authors declare that they have no conflicts of interest in relation to this article.

Data availability statement

The data are available from the corresponding author on request.

References

1. L. Paul: Process of silencing sound oscillations. US Patent 2,043,416, June 9 1936.
2. L.J. Fogel: Apparatus for improving intelligence under high ambient noise levels. US Patent 2,966,549, December 27 1960.
3. D. Crombie: Piano: Evolution, Design and Performance. Barnes and Noble Books, New York, 1995.
4. G.S. Heet: String instrument vibration initiator and sustainer. The Journal of the Acoustical Society of America 65, 6 (1979) 1609–1609.
5. G.T Osborne, A.A Hoover: Sustainer for a musical instrument. US Patent 5,932,827, August 3 1999.
6. H. Boutin: Méthodes de contrôle actif d'instruments de musique. Cas de la lame de xylophone et du violon. PhD thesis, UPMC-Université Paris 6 Pierre et Marie Curie, 2011.
7. T. Meurisse: Contrôle actif appliqué aux instruments de musique à vent. PhD thesis, Paris 6, 2014.
8. C. Maganza, R. Caussé, F. Laloë: Bifurcations, period doublings and chaos in clarinetlike systems. Europhysics Letters 1, 6 (1986) 295.
9. J.S Lienard: An overview of speech synthesis, in: Spoken Language Generation and Understanding: Proceedings of the NATO Advanced Study Institute held at Bonas, France, June 26–July 7, 1979. Springer, 1980, pp. 397–412. See also [hal-04424757](#) from the same author and coll.
10. V. Martos, H. Boutin, T. Hélie, B. d'Andréa Novel: Radiation impedance control of brass resonators to reshape sounds with vowel spectral envelopes: a numerical study, in: Forum Acusticum 2023: The 10th Convention of the European Acoustics Association, 2023.
11. C. Vergez: Trompette et trompettiste: un système dynamique non linéaire à analyser, modéliser et simuler dans un contexte musical. PhD thesis, Paris 6, 2000.
12. N. Lopes: Approche passive pour la modélisation, la simulation et l'étude d'un banc de test robotisé pour les instruments de type cuivre. PhD thesis, Université Paris 6 (UPMC), 2016.
13. J.D. Polack: Time-domain solution of Kirchhoff's equation for sound propagation in viscothermal gases: a diffusion process. Journal d'acoustique (Les Ulis) 4 (1991) 47–67.
14. D. Matignon: Représentations en variables d'état de modèles de guides d'ondes avec dérivation fractionnaire. PhD thesis, Paris 11, 1994.
15. T. Hélie: Modélisation physique d'instruments de musique en système dynamique et inversion. PhD thesis, Paris 11, 2002.
16. R. Mignot: Réalisation en guides d'ondes numériques stables d'un modèle acoustique réaliste pour la simulation en temps-réel d'instruments à vent. PhD thesis, Télécom ParisTech, 2009.
17. A. Thibault: Modélisation, analyse et simulation de l'acoustique dissipative dans les tubes poreux ou rugueux: application aux instruments à vent. PhD thesis, Pau, 2023.
18. N. Amir, V. Pagneux, J. Kergomard: A study of wave propagation in varying cross-section waveguides by modal decomposition. Part II. Results. The Journal of the Acoustical Society of America 101, 5 (1997) 2504–2517.
19. L. Menguy, J. Gilbert: Weakly nonlinear gas oscillations in air-filled tubes; solutions and experiments. Acta Acustica United with Acustica 86, 5 (2000) 798–810.
20. R. Msallam, S. Dequidt, R. Causse, S. Tassart: Physical model of the trombone including nonlinear effects. Application to the sound synthesis of loud tones. Acta Acustica United with Acustica 86, 4 (2000) 725–736.
21. T. Hélie, V. Smet: Simulation of the weakly nonlinear propagation in a straight pipe: application to a real-time

- brassy audio effect, in: 2008 16th Mediterranean Conference on Control and Automation. IEEE, 2008, pp. 1580–1585.
22. M. Campbell, J. Gilbert, M. Arnold: *The Science of Brass Instruments*. Vol. 436. Springer, 2021.
 23. A.P. McPherson: Techniques and circuits for electromagnetic instrument actuation, in: NIME. London, 2012.
 24. J.P. Dalmont, C.J. Nederveen, N. Joly: Radiation impedance of tubes with different flanges: numerical and experimental investigations. *Journal of Sound and Vibration* 244, 3 (2001) 505–534.
 25. F. Silva, P. Guillemain, J. Kergomard, B. Mallaroni, A.N. Norris: Approximation formulae for the acoustic radiation impedance of a cylindrical pipe. *Journal of Sound and Vibration* 322, 1–2 (2009) 255–263.
 26. T. Hélie: *Modélisation physique d’instruments de musique et de la voix: systèmes dynamiques, problèmes directs et inverses*. Habilitation à Diriger des Recherches, 2013, pp. 42–43.
 27. P. Eveno, J.P. Dalmont, R. Caussé, J. Gilbert: Wave propagation and radiation in a horn: comparisons between models and measurements. *Acta Acustica United with Acustica* 98, 1 (2012) 158–165.
 28. T. Hélie, T. Hézard, R. Mignot, D. Matignon: One-dimensional acoustic models of horns and comparison with measurements. *Acta acustica United with Acustica* 99, 6 (2013) 960–974.
 29. S. Mathur, B.H. Story: Vocal tract modeling: implementation of continuous length variations in a half-sample delay Kelly-Lochbaum model, in: *Proceedings of the 3rd IEEE International Symposium on Signal Processing and Information Technology (IEEE Cat. No. 03EX795)*. IEEE, 2003, pp. 753–756.
 30. J.L. Kelly, C.C. Lochbaum: Speech synthesis, in: *Proc. 4th Int. Congr. Acoustics*, Sep. 1962, pp. 1–4.
 31. B.H. Story, I.R. Titze, E.A. Hoffman: Vocal tract area functions from magnetic resonance imaging. *The Journal of the Acoustical Society of America* 100, 1 (1996) 537–554.
 32. H. Boutin, J. Smith, J. Wolfe: Warming up a wind instrument: the time-dependent effects of exhaled air on the resonances of a trombone. *The Journal of the Acoustical Society of America* 148, 4 (2020) 1817–1823.
 33. N. Thiele: Loudspeakers in vented boxes: Part 1. *Journal of the Audio Engineering Society* 19, 5 (1971) 382–392.
 34. R.H. Small: Closed-box loudspeaker systems-part 1: analysis. *Journal of the Audio Engineering Society* 20 (1972) 798–808.
 35. H. Boutin, N. Fletcher, J. Smith, J. Wolfe, Relationships between pressure, flow, lip motion, and upstream and downstream impedances for the trombone. *The Journal of the Acoustical Society of America* 137, 3 (2015) 1195–1209.
 36. M.S. Howe: On the helmholtz resonator. *Journal of Sound and Vibration* 45, 3 (1976) 427–440.
 37. A. Thibault, J. Chabassier: Dissipative time-domain one-dimensional model for viscothermal acoustic propagation in wind instruments. *The Journal of the Acoustical Society of America* 150, 2 (2021) 1165–1175.
 38. V. Välimäki, M. Karjalainen: Improving the Kelly-Lochbaum vocal tract model using conical tube sections and fractional delay filtering techniques, in: *ICSLP*, 1994.
 39. A. Chaigne: *Ondes acoustiques*. Editions Ecole Polytechnique, 2001.
 40. R. Caussé, J. Kergomard, X. Lurton: Input impedance of brass musical instruments – comparison between experiment and numerical models. *The Journal of the Acoustical Society of America* 75, 1 (1984) 241–254.
 41. J.C. Lagarias, J.A. Reeds, M.H. Wright, P.E. Wright: Convergence properties of the nelder-mead simplex method in low dimensions. *SIAM Journal of Optimization* 9, 1 (1998) 112–147.

Cite this article as: Martos V. Boutin H. Hélie T. & d’Andréa-Novel B. 2025. Electro-acoustic control of radiation impedance for brass instrument timbre shaping: design of a vocalizing mute. *Acta Acustica*, 9, 40. <https://doi.org/10.1051/aacus/2025020>.

Table B.1. Characteristics of the trombone resonator used for simulation. These values are taken from the optimisation calculation [41], see Appendix F.

Name	Symbol	Value	Unit
Bore radius	r_b	$6.7 \cdot 10^{-3}$	m
Bore section	$S_b = \pi r_b^2$	$1.57 \cdot 10^{-4}$	m ²
Segment length	d	$3.85 \cdot 10^{-3}$	m
Bore length	$l_1 = 141 \cdot d$	0.5435	m
Bell length	$l_{\text{bell}} = 450 \cdot d$	1.7347	m

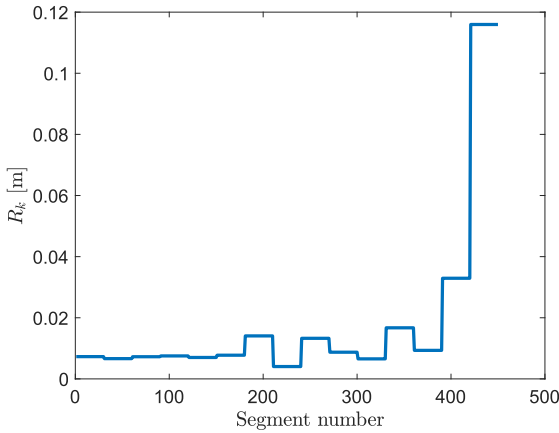


Figure B.2. Profile of the bell.

The acoustics of the complete pipe is then described by

$$X_0 = T_{\text{pipe}} X_N \text{ with } T_{\text{pipe}} = T_1 T_2 \dots T_N, \quad (\text{B.2})$$

the Kelly-Lochbaum structure of which is recalled below in Appendix D.

In a real trombone, the cylindrical bore is followed by the flare, almost conical part, and then the bell, more rapidly flaring part. Accordingly, in our model, the bore is modelled as a straight tube ($n = 1$) with a constant cross section area equal to πr_b^2 , see Figure B.1. For the sake of simplicity, the flared part of the resonator hereafter called “the bell” is composed of a succession of N_{bell} short straight tubes subsequently called segments of equal length d .

Note that for the following simulations: (i) d is chosen so that the propagation time in each tube is half a sampling period [14]; (ii) the length of the bore l_1 is a multiple of d . In addition, the tubes radii in the resonator are chosen such that their rate of increase along the bore exceeds -13.64% , minimum spatial derivative of the radius reported in [40] on a measured trombone bore profile (Courtois TB 14, France).

These parameters result from an optimisation procedure [41], which minimises the distance between the input impedance peaks 2 to 6 of our model ($F_k, k \in [6, 40]$), to those of a real bass trombone ($F_k, k \in [6, 40]$) with the slide in first position, measured in a previous study [35] (Yamaha YBL 321, Hamamatsu, Japan). The optimisation criterion does not concern the first impedance peak, which is generally not played because its harmonics do not coincide with the following peaks.

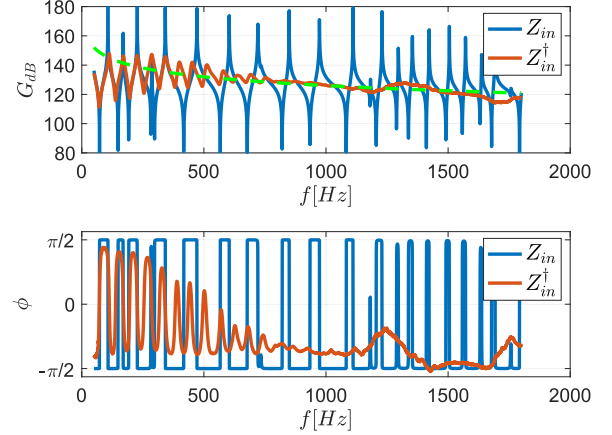


Figure C.1. Modulus (top) and phase (bottom) of measured (red) and modelled (blue) trombone input impedance. The mouthpiece effect appears in the higher frequency range, when the modulus tends to -20 dB/dec asymptotic curve (green) and the phase tends to $-\pi/2$.

Table B.1 gives the numerical values of the above-mentioned physical parameters of the resonator. The resulting profile of the bell is shown in Figure B.2: the 450 segments of equal length d verifying the relationship $l_{\text{bell}} = 450 \cdot d$ are represented. Their radii take on 15 different values, each repeated 30 times to facilitate optimisation. Radius values are reported in Table B.2.

Appendix C Global transfer functions

Assembling the mouthpiece (T_a), the pipe (T_{pipe}) and the radiation load (Z_R) leads to the transfer relation (denoting

$$X_{\text{out}} = \begin{bmatrix} P_{\text{out}} \\ U_{\text{out}} \end{bmatrix} = X_N), \text{ from (B.2) and (A.3):}$$

$$X_{\text{in}} = T_{\text{tb}} X_{\text{out}}, \quad (\text{C.1a})$$

$$\text{with } T_{\text{tbn}} = T_a T_{\text{pipe}} \text{ and } X_{\text{out}} = \begin{bmatrix} Z_R \\ 1 \end{bmatrix} U_{\text{out}}. \quad (\text{C.1b})$$

The input impedance $Z_{\text{in}} = P_{\text{in}}/U_{\text{in}}$ is then given by

$$Z_{\text{in}} = \frac{T_{\text{tb}}^{11} Z_R + T_{\text{tb}}^{12}}{T_{\text{tb}}^{21} Z_R + T_{\text{tb}}^{22}}. \quad (\text{C.2})$$

Figure C.1 compares Z_{in} with the measured input impedance Z_{in}^\dagger of the real bass trombone considered for the optimisation in Section B (see [35]).

It appears that the Q -factors of the resonances are greater in Z_{in} than in Z_{in}^\dagger , as the model does not take viscothermal losses into account. Above the cut-off frequency, the impact of mouthpiece compliance on the input impedance is therefore lower in the model than in the measurement. This explains why the resonance Q -factors are greater in the model, even in the higher frequency range.

Table C.1 presents the amplitude and frequency differences of peaks 2 to 6 between the model Z_{in} and the measurement Z_{in}^\dagger .

Table B.2. Comparison of the values of the 15 radius R_k and their rate of increase. As shown in Figure B.2, the radius profile increases overall. A previous measurement [40] report a comparable radius profile, ranging from 6.9 mm to 101.8 mm with a rate of increase, that can be negative, but always bigger than -13.64% .

k	1	2	3	4	5	6	7	8	9	10	11	12	13	14	15
R_k [mm]	7.07	7.15	7.89	7.10	7.21	6.92	13.55	4.85	10.52	12.30	6.22	16.72	7.59	36.66	110.30
$\frac{R_k - R_{k-1}}{d}$	×	+0.07%	+0.64%	-0.68%	+0.09%	-0.25%	+5.74%	-7.52%	+4.90%	+1.54%	-5.26%	+9.49%	-7.44%	+24.28%	+63.71%

Table C.1. Comparison of the frequencies F_k and amplitudes A_k of the first five peaks Z_{in}^\dagger and Z_{in} .

k	1	2	3	4	5
F_k^\dagger [Hz]	112.376	169.574	226.772	286.661	341.84
A_k^\dagger [dB]	147.867	146.212	146.63	147.294	145.778
$F_k^\dagger - F_{k-1}^\dagger$ [Hz]	×	57.198	57.198	59.889	55.179
F_k [Hz]	108.339	172.939	228.117	290.698	343.858
A_k [dB]	171.039	174.805	172.307	152.902	182.28
$F_k^\dagger - F_{k-1}^\dagger$ [Hz]	×	64.6	55.178	62.581	53.16
$\frac{F_k - F_k^\dagger}{F_k^\dagger}$	-3.59%	+1.99%	+0.59%	+1.41%	+0.59%
$\frac{A_k - A_k^\dagger}{A_k^\dagger}$	+15.67%	+19.56%	17.51%	+3.81%	+25.04%

Appendix D Kelly-Lochbaum structure

The Kelly-Lochbaum structure governs travelling wave variables. Consider the n th elementary straight pipe with characteristic impedance $Z_n = \rho_0 c_0 / A_n = Y_n^{-1}$. The travelling wave signals at its left side are $P_n^{\pm} = (P_{n-1} \pm Z_n U_{n-1})/2$, those at its right side are $P_n^{\pm} = (P_n \pm Z_n U_n)/2$, and they are related by a pure delay, called D_n (see Fig. D.1):

$$\begin{bmatrix} P_n^{r+} \\ P_n^{l-} \end{bmatrix} = D_n \begin{bmatrix} P_n^{l+} \\ P_n^{r-} \end{bmatrix} \text{ with } D_n(s) = e^{-\frac{sd}{2c}}. \quad (\text{D.1})$$

Between pipes n and $n+1$, expressing P_{n+1}^{l+} and P_n^{r-} as functions of P_n^{r+} and P_{n+1}^{l-} yields the structure of junction J_n detailed in Figure D.1 and involved in Figure 14, where the constant reflection coefficients k_n are

$$k_n = \frac{Z_{n+1} - Z_n}{Z_{n+1} + Z_n}. \quad (\text{D.2})$$

At the trombone input, the relation between X_{in} and P_1^\pm is described by

$$\underbrace{\begin{bmatrix} P_{in} \\ U_{in} \end{bmatrix}}_{X_{in}} = T_a \underbrace{\begin{bmatrix} P_0 \\ U_0 \end{bmatrix}}_M = T_a \underbrace{\begin{bmatrix} 1 & 1 \\ Y_1 & -Y_1 \end{bmatrix}}_M \begin{bmatrix} P_1^{l+} \\ P_1^{l-} \end{bmatrix}, \quad (\text{D.3})$$

with, from (A.3),

$$M = \begin{bmatrix} 1 + \alpha Y_1 & 1 - \alpha Y_1 \\ \beta + (1 + \alpha\beta)Y_1 & \beta - (1 + \alpha\beta)Y_1 \end{bmatrix}. \quad (\text{D.4})$$

The transfer functions A , B , C , D involved in Figure 14 are derived from the elements of M , by expressing P_{in} and P_1^{l+} as functions of U_{in} and P_1^{l-} . Computations yield:

$$\begin{aligned} A &= \frac{1}{M_{21}}, \quad B = -\frac{M_{22}}{M_{21}}, \quad C = -\frac{\det(M)}{M_{21}}, \\ D &= \frac{M_{11}}{M_{21}}, \end{aligned} \quad (\text{D.5})$$

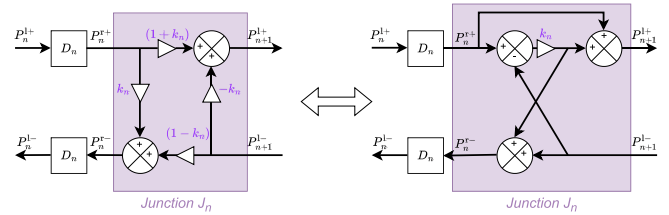


Figure D.1. Kelly-Lochbaum structure of a segment, composed of two delays $D_n(s)$, and a junction J_n , that governs travelling wave signals (see Appendix E for detailed computations). On the left: the schematic diagram of the junction; on the right: the equivalent way in which the junction is implemented.

Table D.1. Expressions of the transfer functions A , B , C and D defined in (D.5) for the mouthpiece (left-hand column) and the vocal tract (right-hand column). These transfer functions give the pressure travelling waves at the inlet to the first tube of the Kelly-Lochbaum structure in Figure 14, with respect to the input pressure and flow.

	Mouthpiece (Sect. D)	Vocal Tract (Sect. 3.2)
A	$\frac{1}{\beta + (1 + \alpha\beta)Y_1}$	Z_1
B	$-\frac{\beta - (1 + \alpha\beta)Y_1}{\beta + (1 + \alpha\beta)Y_1}$	1
C	$\frac{2Y_1}{\beta + (1 + \alpha\beta)Y_1}$	2
D	$\frac{1 + \alpha Y_1}{\beta + (1 + \alpha\beta)Y_1}$	Z_1

the detailed expressions of which are given in the left-hand column of Table D.1.

At the trombone output, $P_N = Z_R U_N$ so that signals $P_N^{r\pm} = (P_N \pm Z_N U_N)/2$ equal $(Z_R U_N \pm Z_N U_N)/2$. Then,

the reflection function $R = P_N^{r-}/P_N^{r+}$ in Figure 14 is given by

$$R(s) = \frac{Z_R(s) - Z_N}{Z_R(s) + Z_N}, \quad (\text{D.6a})$$

which is similar to (D.2) but not constant, and the transmission function $T = P_N/P_N^{r+} = (P_N^{r+} + P_N^{l-})/P_N^{r+} = 1 + R$ is given by

$$T(s) = \frac{2Z_R(s)}{Z_R(s) + Z_N}, \quad (\text{D.6b})$$

Appendix E Coefficient relations

We note the demonstration of the coefficient relations exposed in Figure D.1. Pressure in n th segment P_n is computed from the left-progressive one of the $(n+1)$ th segment noted P_{n+1}^{l+} and from the left-regressive one of the $(n+1)$ th segment noted P_{n+1}^{l-} . Flow rate is deduced thanks to the impedance relation. We obtain:

$$\begin{cases} P_n = P_{n+1}^{l+} + P_{n+1}^{l-} \\ Z_{n+1}U_n = P_{n+1}^{l+} - P_{n+1}^{l-}. \end{cases} \quad (\text{E.1})$$

The same relation can be exposed on the right-side of the segment,

$$\begin{cases} P_n = P_n^{r+} + P_n^{r-} \\ Z_nU_n = P_n^{l+} - P_n^{r-}. \end{cases} \quad (\text{E.2})$$

Using (E.1) and (E.2), we can express P_n^{r-} as a function of P_n^{r+} and P_{n+1}^{l-} ,

$$\begin{aligned} P_n^{r-} &= P_n - P_n^{r+} \\ &= P_{n+1}^{l+} + P_{n+1}^{l-} - P_n^{r+} \\ &= Z_{n+1}U_n + 2P_{n+1}^{l-} - P_n^{r+} \\ &= \frac{Z_{n+1}}{Z_n} (P_n^{r+} - P_n^{r-}) + 2P_{n+1}^{l-} - P_n^{r+}, \end{aligned}$$

by regrouping the following terms,

$$\begin{aligned} \Leftrightarrow P_n^{r-} \left(1 + \frac{Z_{n+1}}{Z_n}\right) &= \left(\frac{Z_{n+1}}{Z_n} - 1\right) P_n^{r+} + 2P_{n+1}^{l-} \\ \Leftrightarrow P_n^{r-} &= \frac{Z_{n+1} - Z_n}{Z_{n+1} + Z_n} P_n^{r+} + \frac{2Z_n}{Z_{n+1} + Z_n} P_{n+1}^{l-}. \end{aligned}$$

As a result, a k_n coefficient is expressed,

$$P_n^{r-} = k_n P_n^{r+} + (1 - k_n) P_{n+1}^{l-}, \quad (\text{E.3})$$

with $k_n = \frac{Z_{n+1} - Z_n}{Z_{n+1} + Z_n}$.

Table F.1. List of the chosen parameters for simulations. The choices of L_{bell} and N_{bore} are explained below.

Resonator	
f_0	37.3 Hz
f_p	$(2p+1) \frac{c_0}{4L_{\text{tot}}}$
$d = \frac{c}{2f_s}$	3.8548 mm
$L_{\text{tot}} = (2p+1) \frac{c_0}{4f_p}$	2.2768 m
$N_{\text{tot}} = \frac{L_{\text{tot}}}{d} = \frac{3f_s}{2f_1}$	561
Bell	
L_{bell}	1.7347 m
$N_{\text{bell}} = \frac{L_{\text{bell}}}{d}$	450
Bore	
$L_{\text{bore}} = L_{\text{tot}} - L_{\text{bell}}$	0.5435 m
$N_{\text{bore}} = \frac{L_{\text{bore}}}{d}$	141

Appendix F Optimisation

The length of the resonator L_{tot} is chosen to fix the first harmonic peak at 37 Hz. As an open/close pipe, its resonance frequencies follow the relation $f_p = (2p+1) \frac{c_0}{4L_{\text{tot}}}$. The length of a straight pipe is equal to d (see Sect. 3.2). So, the number of straight pipes must be equal to 560.6, approximating to $N_{\text{tot}} = 561$ (this approximation gives $f_1 = 111.92$ Hz, which corresponds to a relative error of 0.018%). As N_{tot} , N_{bell} must be an integer, i.e., $2f_s L_{\text{bell}}/c_0 \in \mathbb{N}$. Moreover, the optimisation algorithm is based on a target of a 15-radius model. For this reason, N_{bell} must therefore be an integer and a multiple of 15. These conditions led us to choose $N_{\text{bell}} = 30 \times 15 = 450$. Table F.1 summarises the values chosen to the algorithmic optimisation.